

*From A to ZIF: Amorphous precursors drive nucleation and growth of nanocrystalline ZIF-8*

A. Dok, S. Radhakrishnan, F. de Jong, E. Becquevort, O. Deschaume, Vinod Chandran C., Y. de Coene, C. Bartic, M. Van der Auweraer, W. Thielemans, C. Kirschhock, M. van der Veen, T. Verbiest, E. Breynaert, S. Van Cleuvenbergen

*Nucleation, the pivotal first step of crystallization, governs essential characteristics of crystallization products, including size distribution, morphology, and polymorphism. While understanding this process is paramount for the design of chemical, pharmaceutical and industrial production processes, major knowledge gaps remain, especially with respect to crystallization of porous solids. Also for nanocrystalline ZIF-8, one of the most widely studied metal-organic frameworks, questions regarding the species involved in the nucleation pathway and their structural and chemical transformations remain unanswered. By combining harmonic light scattering, inherently sensitive to structural changes, with NMR spectroscopy, which reveals molecular exchanges between particles and solution, we were able to capture the crystallization mechanism of ZIF-8 in unprecedented detail. Initially, oligomerization forms small, prenucleation clusters with an excess of protonated ligands in a pre-equilibrium state. When these clusters aggregate to form amorphous precursor particles, protonated ligands are released, leading to an amorphous charge neutral structure that subsequently transforms into crystalline ZIF-8 through intraparticle reorganization. Later stages involve solution-mediated Ostwald ripening, where the growth mechanism changes to incorporation of monomers from solution. Our results demonstrate the intricate link between charge, stoichiometric and structural evolution in MOFs, and open up pathways for managing crystallization through chemical control of precursor phases.*

## 1. Introduction

Metal-organic frameworks (MOFs) are a class of crystalline materials that form nanoporous networks by interconnection of metal-based nodes with polydentate organic ligands. Owing to their large surface area and intrinsic structural and functional diversity, MOFs can be tuned for specific applications including gas storage, separation, and catalysis. This has led to a tireless exploration of the MOF material space, with nearly a hundred thousand structures reported so far.<sup>1</sup> The concept of secondary building units (SBUs) has served as a basis to guide this endeavor.<sup>2</sup> However, despite the success of modular chemistry in rationalizing MOF synthesis, there is a gap between the selection of appropriate building blocks and the final crystal product.<sup>3</sup> To date, the discovery and optimization of MOFs have relied heavily on trial and error. In order to bridge this gap, a fundamental understanding of the crystallization process of MOFs is deemed essential.<sup>3</sup>

The nucleation and growth of porous crystals, such as MOFs and zeolites, have become an active research field in recent years. Insights into the thermodynamics, phase transformations, and kinetics have been gained for a number of prominent materials, including relevant energetic barriers and (nonclassical) nucleation and growth mechanisms.<sup>3</sup> In particular, the members of the zeolitic imidazolate framework (ZIF) family, a subclass of MOFs, have attracted significant interest. ZIF-8 is by far the most widely investigated, due to its excellent gas separation abilities, high stability and ease of synthesis. For large-scale production of ZIF-8, fast room-temperature protocols have been developed aimed at the production of nanocrystals in a straightforward, and reproducible manner. However, the upscaling of these synthesis routes is currently hampered by the incomplete knowledge of the crystallization mechanism.<sup>4</sup> Crystallization processes of MOFs typically follow a structured progression involving multiple steps before reaching the final crystalline product, the specific timeline of which can vary significantly depending on the experimental conditions.<sup>5</sup> To effectively optimize and manage these crystallization processes, it is crucial to gain a comprehensive understanding of the sequential events that occur rather than solely focusing on the characterization of the end crystalline product. To accomplish this objective, it is evident that employing experimental approaches that enable *in situ* real-time monitoring of crystallization processes is imperative.

The rapid room-temperature synthesis of ZIF-8 nanoparticles, pioneered in 2009 by Cravillon et al., was achieved in a straightforward manner by mixing an excess of 2-methylimidazole (2-Melm) and  $\text{Zn}(\text{NO}_3)_2 \cdot 6\text{H}_2\text{O}$  in methanolic solution.<sup>6</sup> Since the formation of clusters and crystalline nanoparticles starts almost immediately after mixing, and most of the crystal growth takes place within minutes, the experimental characterization of the crystallization mechanism, especially at the initial stages has proved challenging.<sup>6</sup> Detailed insights into the early stages were obtained through *in situ* synchrotron small- and wide- angle X-ray scattering (SAXS/ WAXS).<sup>7-9</sup> Small-Angle X-ray scattering (SAXS) data showed the formation of a population of clusters with a stable size of about 2 nm almost immediately after mixing, and serving as a reservoir for consequent particle growth.<sup>6-8</sup> The initial structure of the growing particles remained an open question, since WAXS detection of the crystalline framework was slightly delayed with respect to the initial detection of particle formation via SAXS. The authors speculated this might indicate the initial particles were amorphous rather than crystalline.<sup>7</sup> Unfortunately, the time between the onset of the SAXS and WAXS signals was too small with respect to the experimental time resolution to formulate definitive conclusions.<sup>6,7,10</sup> The notion of the potential importance of amorphous precursors is however strengthened by other studies, showing the presence of amorphous domains for ZIF-8 crystallites through ex-situ measurements, or establishing the disordered nature of the small cluster population.<sup>9,11-17</sup> Similar observations regarding the involvement of amorphous precursors were presented for ZIF-8 in aqueous conditions or for ZIF frameworks with different topologies.<sup>5,18-20</sup> For the crystallization of zeolites, analogous two-step nucleation mechanisms involving amorphous precursor particles or ion-paired prenucleation clusters have also been observed.<sup>21-25</sup>

The structural development of ZIF-8 cannot be separated from the chemistry occurring in the mother liquor of the crystals. In case of ZIF-8, a series of ligation and deprotonation reactions results in a complex chemical landscape dominated by monomeric zinc complexes almost immediately after mixing.<sup>9,26</sup> The pathways connecting this diverse pool of dissolved species to the final crystal structure remains a matter of debate.<sup>6,9,26,27</sup> Based on kinetic data and modelling, Yeung et al. proposed that oligomerization predominately starts from complexes that are (sub-)stoichiometric with respect to the final composition of ZIF-8,  $\text{Zn}(\text{Melm})_2$ .<sup>28</sup> This results in oligomeric complexes containing an excess of ligands, which evolve towards the final composition of ZIF-8 by condensation. Another topic of discussion remaining is the homogeneous or heterogeneous nature of nucleation and growth processes. Does nucleation and growth occur in solution, or inside unstructured gel-like particles which

transform into crystalline ZIF-8?<sup>9,26,28,29</sup> This question is closely related to the potential presence of an amorphous precursor phase.<sup>9,26,28</sup>

In this study, a two-tiered approach combining harmonic light scattering experiments and static NMR spectroscopy was adopted to address the lingering questions surrounding crystallization of ZIF-8. Harmonic light scattering was employed to probe the internal structure of the particles, providing insights into their formation from the solid-state perspective. Static NMR spectroscopy was employed to deliver the inverse picture, by selectively probing the evolution of the dissolved chemical species. By combining both techniques a complete picture of all events occurring in the solid and liquid fractions of the system is obtained.

Harmonic light scattering is a nonlinear optical method which is particularly sensitive to the local organization of matter. It allows to examine the supramolecular arrangement of aggregates, clusters, and crystals.<sup>30</sup> For second harmonic scattering (SHS), this structural sensitivity is illustrated most clearly by the effect of an inversion center, which results in an effective cancellation of the response. In other words, SHS detects only non-centrosymmetric structures. In an earlier study, SHS was used to monitor the non-centrosymmetric I-43m space group of ZIF-8 during crystallization.<sup>31</sup> To detect potential amorphous precursor particles, we used third harmonic scattering (THS) as an additional probe in this study. In addition to SHS, THS can identify all the symmetries, making it possible to differentiate between potential amorphous intermediates (via THS) and crystalline ZIF-8 (via both SHS and THS).<sup>32,33</sup> Through polarization measurements, additional information about (point group) symmetry can also be derived.<sup>31,32,34</sup> Owing to their strong dependence on particle size ( $\sim R^6$ ), SHS and THS are primarily sensitive to particles rather than small complexes and oligomers.

Complementary to X-ray scattering and diffraction, in situ NMR spectroscopy enables liquid-state selective monitoring of crystallizing systems. It allows to track solvent dynamics, solute interactions, and the impact of temperature and concentration on crystallization, aiding kinetic modeling. In this work, static NMR spectroscopy was used to monitor the evolution of the concentration and speciation of dissolved ZIF-8 linkers, i.e. unreacted methylimidazole molecules and molecules incorporated in small clusters, thus providing complementary information to the harmonic light scattering experiments.<sup>35-37</sup>

Overall, the combination of NMR and HLS elegantly captures the different stages of ZIF-8 crystallization. Oligomeric clusters serve as reservoirs for particle formation, first transforming into an amorphous network, which, through condensation, evolves into crystalline ZIF-8. As crystallization progresses and the oligomeric reservoir is gradually depleted, the amorphous phase is consumed as the growth mechanism switches to solution-mediated growth, in line with Ostwald ripening.

In what follows, first the theory behind SHS and THS is explained. Subsequently all results obtained by the different techniques are outlined and the accompanying discussion provides an in-depth analysis and interpretation. The discussion further relates the experimental results to the crystallization mechanism of nanocrystalline ZIF-8, situating the observations in the context of current literature.

## 2. Theory

SHS is a nonlinear optical process in which two photons of frequency  $\omega$  interact simultaneously with a material to create a new photon at double the frequency  $2\omega$ . Analogously, for THS, a three photon interaction results in a photon at triple frequency  $3\omega$ . To overcome the low probability of both processes, SHS and THS typically require illumination with pulsed laser light of much higher intensity compared to classical (linear) light scattering.

For nanoparticles that are small compared to the wavelength of the incident light, as is the case in this study (see ESI.1a), hyper-Rayleigh scattering ensues. In this regime scattering is isotropic, meaning that the light intensity is identical for all scattering angles in the case of vertically polarized incident light. The total scattering intensity is then found as the incoherent sum over all particles:

$$I_{\text{SHS}} \sim N \langle |\chi_{\text{HRS}}^{(2)}|^2 \rangle \langle V^2 \rangle I_{\omega}^2 \quad (1)$$

$$I_{\text{TSHS}} \sim N \langle |\chi_{\text{HRS}}^{(3)}|^2 \rangle \langle V^2 \rangle I_{\omega}^3 \quad (2)$$

SHS and TSHS are linearly related to the particle concentration  $N$  and quadratically to the orientationally averaged second and third susceptibility. Within the electric dipole approximation, SHS is forbidden for structures with inversion symmetry, as the second susceptibility  $\chi^{(2)} = 0$  in this case. In contrast to SHS, there are no symmetry restrictions for TSHS. For a single particle the intensity of both processes scales with the particle volume squared. For a collection of particles with a distribution of sizes, the intensity is therefore related to the average of the volume squared.

The scattering intensities for second- and third order processes are additive. As a result, all solution species will in principle contribute to the measured scattering intensity. Equations 3 and 4 describe the total SHS and TSHS intensity found for a generalized crystallization process:

$$I_{\text{SHS}} \sim (\sum_m N_m \langle |\beta_{\text{HRS},m}^{(2)}|^2 \rangle + \sum_{\text{ncs},i} N_i \langle |\chi_{\text{HRS},i}^{(2)}|^2 \rangle \langle V_i^2 \rangle) I_{\omega}^2 \quad (3)$$

$$I_{\text{TSHS}} \sim (\sum_n N_n \langle |\gamma_{\text{HRS},n}^{(3)}|^2 \rangle + \sum_{\text{ncs},i} N_i \langle |\chi_{\text{HRS},i}^{(3)}|^2 \rangle \langle V_i^2 \rangle + \sum_{\text{cs},j} N_j \langle |\chi_{\text{HRS},j}^{(3)}|^2 \rangle \langle V_j^2 \rangle) I_{\omega}^3 \quad (4)$$

These equations encompass the response of all solution species. Molecular species (like solvent and linker) react as per  $\beta^{(2)}$  and  $\gamma^{(3)}$ , their first and second hyperpolarizabilities. Macroscopic clusters and particles respond through their macroscopic susceptibilities  $\chi^{(2)}$  and  $\chi^{(3)}$ . We have distinguished centrosymmetric (cs) and non-centrosymmetric (ncs) macroscopic contributions; the former contributing exclusively to TSHS, while the latter affects both SHS and TSHS. Notably, in crystallization, macroscopic responses ( $\chi^{(2)}$ ,  $\chi^{(3)}$ ) often overshadow molecular ones ( $\beta^{(2)}$ ,  $\gamma^{(3)}$ ) early in the process, due to their volume-squared dependence.

Due to the tensorial nature of the first and second hyperpolarizability for molecules, and the second and third susceptibility for particles, polarized measurements contain additional information regarding the symmetry of species. In this study, the depolarization ratio  $\rho$ , defined as the ratio between the intensity of cross-polarized and parallel-polarized SHS and TSHS light, is used to interrogate symmetry.<sup>30,38,39</sup>

$$\rho_{\text{SHS}} = \frac{I_{\text{HV}}(2\omega)}{I_{\text{VV}}(2\omega)} \quad (5)$$

$$\rho_{\text{TSHS}} = \frac{I_{\text{HV}}(3\omega)}{I_{\text{VV}}(3\omega)} \quad (6)$$

In these equations the first subscript refers to the polarization of the scattered light, the second to the polarization of the incident light. H stands for horizontal polarization, V for vertical polarization. The SHS depolarization ratio ranges from 1/9 for dipolar to 2/3 for octupolar species. For ZIF-8, which has octupolar  $T_d$  symmetry (I-43m space group), the depolarization ratio assumes a value of 2/3. In TSHS, this ratio varies from 5/8 for hexadecapolar symmetry to 0 for isotropic species. For amorphous particles a depolarization ratio of exactly 0 is expected. For  $T_d$  symmetry there is no exact solution. However, an almost isotropic response, with values near 0, can generally be assumed.

### 3.Results

**Formation of particles measured by light scattering.** The fast crystallization of ZIF-8 in methanol was measured in-situ with a range of time-resolved scattering techniques for a molar ratio of 1:4:1000 (Zn: MeImH:MeOH). Static light scattering (SLS), SHS and THS were measured in parallel for the same synthesis using a pulsed laser source at 1260 nm, while DLS measurements were performed separately under the same conditions using a continuous 543 nm laser source. The synthesis protocol is highly reproducible when starting from the same reagent and solvent batches. Between solvent batches small variations in induction times were observed, but overall the data shows the same trends. Differences are most likely linked to small differences in water content. (see ESI.3.8). Figure ESI.3.4 presents the time evolution of the normalized intensity of LS, SHS and THS scattering. Due to the inherent confocal effect of SHS and THS,<sup>34</sup> LS probes a much larger volume than SHS and THS and consequently it is more sensitive to multiple scattering effect (See Fig. ESI.3.6). To limit the impact of multiple scattering effects (due to particle aggregation and precipitation) on the data analysis, either through depolarization or intensity fluctuations, the analysis was focused on the first 500 seconds of the synthesis. Both DLS and LS indicated multiple scattering only became significant after this timeframe (See ESI.1a and ESI.3.6). Immediately after mixing, a stable scattering signal was detected for LS and SHS, but not for THS. These signals can be attributed to the molecular (hyper-)Rayleigh scattering stemming mainly from the aromatic 2-Melm linkers and the solvent molecules. After an induction period of 52s, LS is the first to pick up on a sharp increase in scattering signal. THS and SHS register a rapid increase in signal after approximately 72 and 84 seconds. It is noteworthy that after the steep initial increase, reminiscent of burst nucleation, the curves do not plateau in the typical sigmoidal manner expected for classical nucleation and growth. Indeed, while the process decelerates after approximately 200 seconds, all scattering signals still display a marked increase in intensity, by a factor of 2.4, 2.7 and 2.3 for LS, SHS and THS respectively between 200 and 500 seconds.

Time-resolved DLS measurements, performed under identical synthesis conditions and using finest possible time-resolution yielding a reasonable signal to noise ratio, allowed to track the evolution of particle size. Figure 2a shows the evolution of the growing ZIF-8 nanoparticles with time.

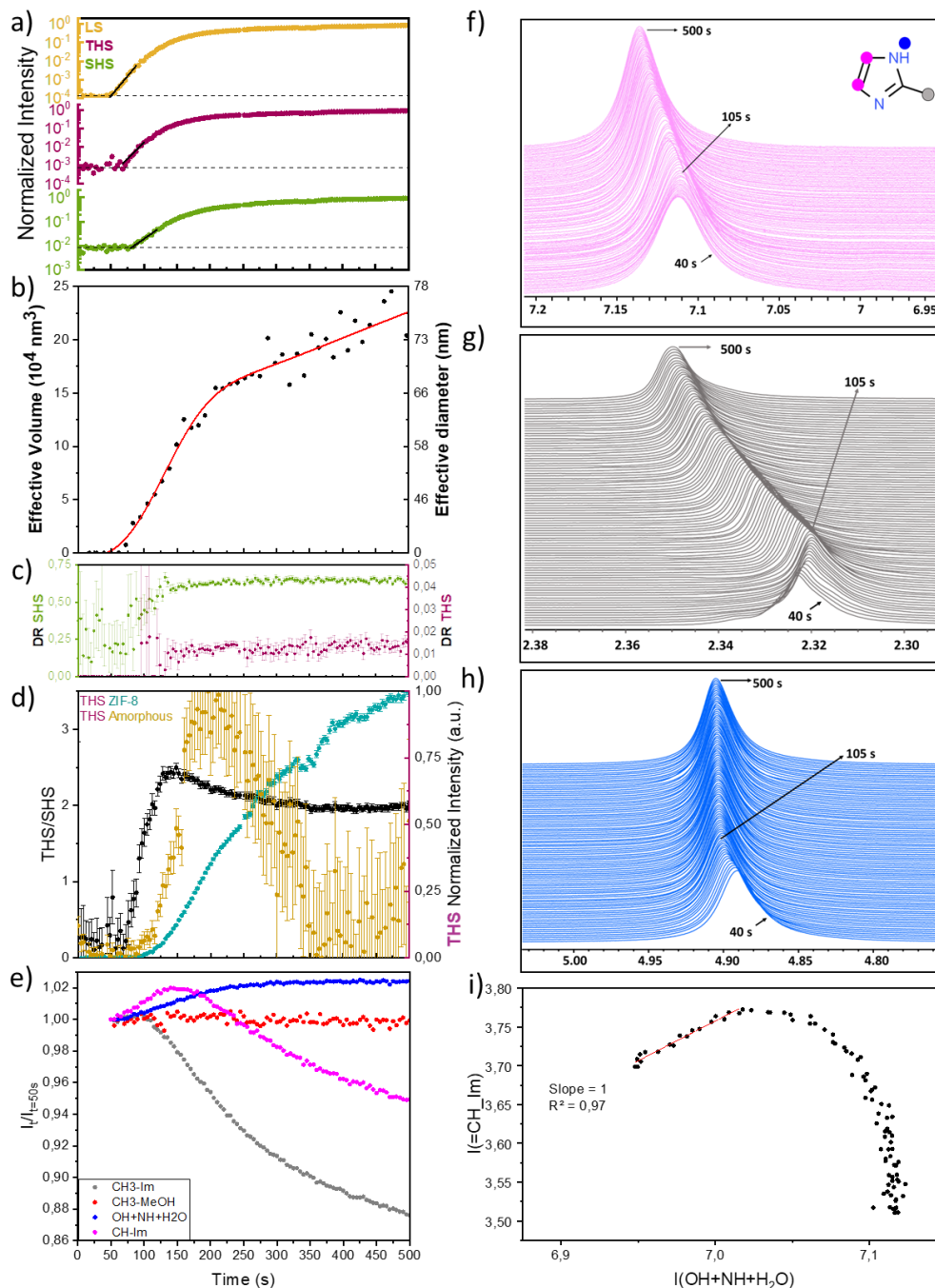


Figure 1: Time-resolved, in situ light scattering and NMR spectroscopy data collected during the crystallization of ZIF-8 from a 1:4 molar mixture of  $Zn(NO_3)_2$  and 2-methylimidazole. **a.** Evolution of effective diameter and averaged particle volume obtained by DLS (points) and a Lifshitz and Slyozov model fit (red line) describing the data as a combination of sigmoidal Avrami growth curve, followed by Ostwald ripening. **b.** Normalized total scattering intensity (VH+VV scattering) for LS, SHS and THS. The onset of the scattering for all harmonics was determined by intersecting a linear fit of the initial onset (black line) with the mean scattering intensity before onset (dashed line). Details are provided in ESI.3.5 **c.** Time-resolved depolarization ratio for SHS (green) and THS (purple) and THS. **d.** black curve: Time-evolution of the THS/SHS ratio for ZIF-8 crystal growth (left y-axis). THS and SHS signals onset around 70 and 80s respectively. brown and green curves: THS scattering intensity evolution of the amorphous and crystalline fractions (right y-axis). **e.** Time-evolution of the normalized ( $T=50s$ ), integrated area of  $^1H$  NMR resonances associated to the methyl protons of methanol (black) and imidazole (red), exchangeable protons (blue) and 2-methylimidazole CH protons (pink). **f,g.** Time evolution of the  $^1H$  NMR resonances of respectively the olefinic protons of 2-methylimidazole and the composite resonance of exchangeable protons (NH, OH and  $H_2O$ ). **h.** Time evolution of the  $^1H$  NMR resonance of the methyl resonance of 2-methylimidazole. **i.** correlation plot of the normalized integrals of the olefinic  $^1H$  resonance of 2-methyl imidazole plotted (y-axis) and the composite resonance of exchangeable protons (x-axis). The synthesis time evolves from left to right. The red line indicates a linear fit in the timeframe between 40 and 135.

The first particles could be detected around 50 seconds. At 70 seconds, a diameter around 40 nm was determined with good accuracy. Thereafter, the effective particle diameter continuously increased until a size of about 65 nm was reached around 200 seconds. After that point, the particle size increased at a slower rate up to 80 nm at 500 s. These results are in line with SLS measurements by Cravillon et al., who observed only minor changes in the overall size of ZIF-8 nanocrystals after 130 seconds under the same conditions.<sup>6</sup> The observed stages could be attributed to a nucleation and growth process followed by Ostwald ripening by fitting to a combined Johnson–Mehl–Avrami–Kolmogorov (JMAK) and Lifshitz-Slyozov model:<sup>40</sup>

$$V(t) = \left( \left\{ 1 - \exp\left[-(k_g t)^n\right] \right\} + \left\{ \frac{t - \tau_{OR}}{1 + \exp[-2\omega(t - \tau_{OR})]} \right\} k_{OR} \right) V_{lim} \quad (7)$$

The first term in equation 7 follows from the Johnson–Mehl–Avrami–Kolmogorov (JMAK) equation, with  $k_g$  a growth rate constant and  $n$  the Avrami exponent. The second term describes Ostwald ripening, with  $k_{OR}$  the rate constant and  $\tau_{OR}$  the onset time. The fitted values for  $k_g$  and  $n$  are  $0.40 \text{ min}^{-1}$  and 2.8 respectively. The Ostwald ripening term of the fitted model resulted in a value of  $\tau_{OR}$  of 195 seconds. This is the onset time indicating the end of particle growth and the start of the Ostwald ripening stage.<sup>40</sup> The Avrami coefficient obtained through DLS is significantly higher than a value determined by WAXS measurements for the same synthesis.<sup>3,41</sup> Since WAXS exclusively detects the crystalline phase, this mismatch may point to the presence of additional phases detected by DLS. Note that the interpretation of the Avrami exponent with respect to the crystallization mechanism is generally considered problematic for solution crystallization processes.<sup>41</sup> Moreover, the JMAK model does not specify the nucleation mechanism, which could be classical or non-classical.

Unlike conventional light scattering techniques, HLS provides a qualitative measure of the symmetry of the scattering species during the crystallization process through measurement of the depolarization ratio  $\rho$ . We find that SHS detects the crystalline ZIF-8 framework, while THS is in line with both amorphous or crystalline ZIF-8 particles.

Figure 2c shows the evolution of  $\rho_{SHS}$  and  $\rho_{THS}$ . Immediately after mixing,  $\rho_{SHS}$  has a value of  $\sim 0.3$ . This value reflects the symmetry of the 2-Melm linkers,<sup>31</sup> demonstrating that these species initially dominate the SHS response. When the SHS signal starts to increase rapidly around 84 seconds,  $\rho_{SHS}$  gradually shifts to a value of approximately 0.63 in line with the expected theoretical value of  $2/3$  for the  $T_d$  point group of ZIF-8. This **confirms the formation of crystalline ZIF-8, which was further validated through in situ WAXS**, and through ex situ powder XRD measurements on the final product (ESI.4.1). For THS, which is typically weaker, no measurable signal was detected prior to the onset of particle formation.  $\rho_{THS}$  assumes a value close to 0 throughout the entire process. As laid out in the theory section, such low values for  $\rho_{THS}$  are consistent with the formation of the highly symmetrical structure of ZIF-8 as well as amorphous particles.

Since SHS serves as an exclusive probe of crystalline ZIF-8, while THS probes ZIF-8 as well as amorphous particles, comparison of both responses can reveal potential contributions of an amorphous precursor. We introduce the THS to SHS ratio for this purpose. Based on equations 3 and 4,  $THS/SHS$  can be reduced to:

$$\frac{THS}{SHS} \sim \frac{\sum_{zif-8,i} N_i \langle |X_{HRS,i}^{(3)}|^2 \rangle \langle V_i^2 \rangle + \sum_{a,j} N_j \langle |X_{HRS,j}^{(3)}|^2 \rangle \langle V_j^2 \rangle}{\sum_{zif-8,i} N_i \langle |X_{HRS,i}^{(2)}|^2 \rangle \langle V_i^2 \rangle} \quad (9)$$

In this equation, we omitted the negligible molecular contribution of the solvent and the solute linker molecules. Subscripts  $a$  and  $zif-8$  refer to amorphous and crystalline particles (or domains) respectively. Remark that  $THS/SHS$  is proportional to the intensity of the laser source, but since the

intensity remains constant during the measurement  $I_{\omega}$  was omitted. Before discussing the results, it is instructive to consider  $THS/SHS$  within the framework of a classical nucleation process, characterized by the presence of a single crystalline species throughout the entire process. Under such circumstances,  $THS/SHS$  can be reduced to:

$$\left(\frac{THS}{SHS}\right)_{CNT} \sim \frac{N_{zif-8} \langle |x_{HRS,zif-8}^{(3)}|^2 \rangle \langle V_{zif-8}^2 \rangle}{N_{zif-8} \langle |x_{HRS,zif-8}^{(2)}|^2 \rangle \langle V_{zif-8}^2 \rangle} = constant \quad (10)$$

Due to the proportional increase of both the volume and number of particles, a constant value for  $THS/SHS$  is thus expected in case of a classical nucleation scenario (CNT). Stated otherwise, deviations from a constant  $THS/SHS$  point to additional contributions from amorphous intermediates. Contributions from defect formation in the ZIF-8 crystal lattice is not expected, as no deviation from perfect stoichiometry is observed during *ex situ* NMR measurements (ESI.4.2 NMR analysis).

For the synthesis of ZIF-8,  $THS/SHS$  is plotted in Figure 2d. It is clear that  $THS/SHS$  varies significantly over the course of the process, and hence the crystallization cannot be described according to a classical nucleation model. In the initial stage of nucleation and growth,  $THS/SHS$  shoots up sharply, which can only be attributed to additional contributions to the THS signal related to the formation of amorphous species. Even after the formation of crystalline ZIF-8 is picked up by SHS,  $THS/SHS$  keeps increasing. This implies that the amorphous phase develops at a more rapid pace compared to the formation of crystalline ZIF-8. A plot of the growth rate for SHS and THS, calculated as the first derivative of both signals, further corroborates this (Fig. ESI.3.8). Around 150 seconds,  $THS/SHS$  reaches a maximum, after which a gradual decrease ensues. After 350 seconds,  $THS/SHS$  plateaus, as SHS and THS increase proportionally from that point onwards. In other words, after 350 seconds, the amorphous to crystalline transition is complete and SHS and THS exclusively detect the crystalline structure of ZIF-8. We can now write:

$$\left.\frac{THS}{SHS}\right|_{t>350s} = \frac{THS_{zif-8}}{SHS_{zif-8}} = 1.94 \quad (11)$$

Through substitution we can now express the total THS intensity as:

$$THS_{tot} = THS_a + THS_{zif-8} = THS_a + 1.94 \times SHS_{zif-8} \quad (12)$$

Since  $SHS_{zif-8}$  corresponds to the total intensity detected by SHS ( $SHS_{tot}$ ), it becomes possible to separate the contributions of the amorphous and crystalline fraction throughout the process, as plotted in Figure 2d. This paints a comprehensive picture of the crystallization process. The crystallization of nanocrystalline ZIF-8 starts with the formation of an amorphous phase which amplifies throughout the initial stage. Shortly after, crystalline ZIF-8 starts forming at a slower pace. Around 200 seconds, the amorphous fraction reaches a maximum. This coincides with the switch in growth mechanism to Ostwald ripening detected by DLS (Fig. 1b). Further transformation of the amorphous phase ensues until it is completely consumed around 350 seconds. Comparing the THS intensities for the amorphous and the crystalline fraction,  $THS_a$  is notably lower than  $THS_{zif-8}$  throughout the process. This might be related to the relative size of amorphous domains, as THS scales with the volume squared, and to their density, through  $x_{HRS,a}^{(3)}$ .

**Solution chemistry measured by  $^1H$  NMR.** For the *in situ*  $^1H$  NMR investigation into the formation of ZIF-8, solutions of  $Zn(NO_3)_2$  and 2-methylimidazole in methanol- $d_4$  were prepared. Pure 2-Melm dissolved in methanol- $d_4$  exhibits two distinctive  $^1H$  resonances at chemical shifts of 2.3 ppm and 6.8 ppm corresponding to the methyl and olefinic protons, as depicted in Figures 1f and 1g. The FWHM



of these resonances were 2.5 Hz and 2 Hz respectively. Apart from the imidazole resonances, resonances corresponding to methyl groups of residual methanol solvent at 3.3 ppm and the composite resonance of NH of imidazole and OH of methanol at 5 ppm were observed. For *in situ* static  $^1\text{H}$  NMR experiments, the two solutions were mixed in a 1:4 molar ratio in a 5 mm NMR tube (labelled  $t^0$ ) and immediately inserted in the NMR probe head, and spectra were acquired every 5 s and the results are depicted in Figures 1e-i. At  $t^0 + 35$  s, the first qualitative spectrum was acquired and from  $t^0 + 50$  s onwards, the system was shimmed and stabilized enough to enable recording quantitative spectra (Figure 1f-h, Figure S1). This is evidenced by the constant integral for the non-exchangeable methyl proton of the residual protonated methanol in the mixture (Figure 1e, red dots), the smallest mobile molecule in the system, ensuring shim stability, implementation of an appropriate relaxation time and providing an internal reference for quantification. The use of static  $^1\text{H}$  NMR implies that all observed resonances pertain exclusively to mobile protons. This implies the signal exclusively reflects protons in dissolved components and small nanoaggregates: i.e. dissolved  $\text{Zn}^{2+}$ -2-Melm complexes, small aggregates of solvated 2-Melm complexes, free (unreacted) 2-Melm, and exchangeable protons. Upon introduction of  $\text{Zn}(\text{NO}_3)_2$ , the olefinic resonance of 2-Melm underwent substantial alterations, broadening to a FWHM of 40 Hz and shifting to 7.1 ppm (Figure S1). The transition to a higher chemical shift is attributed to the complexation of  $\text{Zn}^{2+}$  ions by 2-methylimidazole. The pronounced broadening results from chemical shift broadening effects arising from the formation of a score of  $\text{Zn}^{2+}$ -2-Melm $^-$  and  $\text{Zn}^{2+}$ -2-MelmH complexes and exchange phenomena between various molecular species within the solution, i.e. 2-MelmH, 2-MelmH $_2^+$ , and 2-Melm $^-$  incorporated in  $\text{Zn}^{2+}$ -complexes, nanoaggregates and potentially the surface species of the solid fraction.

Detailed examination of the evolution of the resonances in the  $^1\text{H}$  spectra revealed concurrent variations in the chemical shifts and integrated area (Figure 1e,i; Figure S1-3). The non-exchangeable methyl proton of the residual methanol solvent served as the internal reference for the quantification (Figure 1e, red dots). In the context of an evolving mixed-phase system, it is important to consider the potential quantification discrepancies that can arise due to the quantum rotor effect of components like methyl. Although methyl species are part of a solid, their dipolar interactions which typically broaden resonances, are partially mitigated by their quantum rotor behavior. This results in enhanced visibility of methyl species compared to others within the solid. Consequently, the methyl resonance of imidazole was excluded from the quantitative analysis. The integrated areas corresponding to the non-exchangeable imidazole olefinic  $^1\text{H}$  resonances displayed an initial increase between the time points of 50 and 100 s, after which the signal plateaued, before starting to gradually decline again at 150 s (Figure 1e, pink dots). This initial increase is indicative of an increase in concentration of mobile (dissolved) 2-Melm molecules. It indicates a release of 2-Melm molecules from an immobile (solid) phase into the liquid phase. Concurrently, the area of the  $^1\text{H}$  resonance associated with the exchangeable protons in the system - the NH, H $_2$ O and OH protons (Figure 1e, blue dots) - steadily increased as function of time up to 200 s after  $t^0$  and then remained constant. This suggests a release of exchangeable  $^1\text{H}$  species from clusters containing immobile and thus invisible 2-Melm molecules. Linear fitting of the increase in the =CH area versus the area of the resonance associated with exchangeable protons reveals a slope of 1, hinting at release of two exchangeable protons per imidazole molecule released (Figure 1i). This is in line with particle growth by condensation via release of MelmH $_2^+$  proposed by Yeung et al.<sup>28</sup> The subsequent decrease after 150 s suggests continuous assimilation of ligand into a solid phase. This aligns with the results of the nonlinear optical studies showing an increase in the crystalline fraction. As the resonance associated with the exchangeable protons in solution remains stable after this point (Figure 1e, blue dots), it can be inferred that the species being incorporated are imidazolate moieties (2-Melm $^-$ ). The observed changes in the  $^1\text{H}$  chemical shifts also provides similar picture (Figure 1f-h). The olefinic resonance initially underwent a

subtle shift to lower chemical shift, primarily up to 100 s after  $t^0$ , followed by a progressive transition to higher chemical shift (Figure 1f). The initial effect is attributed to the increased presence of free 2-Melm molecules. The transition after 100 s aligns with the crystallization of the solid fractions, indicative of intensified interactions of the 2-Melm moieties with  $Zn^{2+}$  species and the solid constituents. The composite resonance corresponding to the OH+NH+H<sub>2</sub>O resonances initially also showed an evolution towards higher chemical shift, consistent with the release of 2-MelmH<sub>2</sub><sup>+</sup> (Figure 1h).

*In situ* <sup>1</sup>H NMR spectroscopy thus provides complementary information about the reagents in the mixture and their evolution with time, compared to the light scattering experiments exclusively looking at bigger clusters and solid particles, and assist in obtaining a more complete picture of the crystallization process. The results of <sup>1</sup>H NMR spectroscopy indicate the formation of oligomeric species upon mixing, which are not detectable in the static NMR spectrum. NMR points towards the release the 2-MelmH<sub>2</sub><sup>+</sup> moiety from these oligomers during the particle growth phase and suggest that the predominant imidazole species assimilated in the crystalline ZIF-8 formation phase is 2-Melm<sup>-</sup>. The timescales of these findings are in alignment with that observed in the light scattering experiments. In a separate *ex situ* experiment, the amount of linker in the synthesized ZIF-8 was quantified and found to be very close to the linker quantity expected for a perfect material, indicating no major defects were present in the final product. This quantitative NMR experiment required less sample than the standard thermogravimetric analysis approach.

## Discussion

Based on our results, we identified four key stages in the nucleation and growth mechanism of nanocrystalline ZIF-8 in methanol, which will be discussed in detail below. The onset of these stages ( $\tau_p$ ,  $\tau_{ZIF-8}$ ,  $\tau_{OR}$ ) are indicated in Fig. 1. Immediately after mixing, complexation leads to the formation of prenucleation clusters, as detected by NMR. At  $\tau_p$  (50 s), the growth of the first particles is detected by SLS. At  $\tau_{ZIF-8}$  (85 s), the appearance of crystalline ZIF-8 is confirmed through SHS measurements. Finally, at  $\tau_{OR}$  (200s), the onset of Ostwald ripening is detected by a fit to the DLS data.

Prior to the detection of the first particles at  $\tau_p$ , Static <sup>1</sup>H NMR spectroscopy is highly sensitive to dissolved and very small mobile species. However, as it takes some time to achieve a B<sup>0</sup> field homogeneity, quantitative results were only acquired from  $\tau_p$  onwards. Static <sup>1</sup>H NMR measurements nevertheless indirectly provided information about the chemical species formed prior to  $\tau_p$ . Contrary to expectations, the detection of the first particles coincided with an increase in the concentration of mobile imidazole in the solution (Fig. 1e). Since NMR exclusively detects species in free exchange with the solution and not those that are part of larger structures, this implies that the imidazole molecules were initially immobilized in extended clusters, and subsequently released into solution. Different studies have demonstrated that a diverse array of complexes, varying in coordination geometry and the number of coordinating imidazole molecules, forms almost immediately after mixing.<sup>9,26,41,42</sup> In the case of ZIF-8 synthesis in methanol, using a 1:4 metal to linker ratio, ESI-MS identified monomeric tetrahedral complexes with three methylimidazole ligands as the predominant species, aligning with similar findings in Co ZIF-67.<sup>26</sup> Alongside these small complexes, the formation of non-crystalline clusters preceding particle growth, a few nanometers in size, has been detected by synchrotron based experiments.<sup>9,18,29</sup> Since static <sup>1</sup>H NMR is able to detect ligands present in monomeric complexes but not in extended structures, it follows that these clusters act as the source of imidazole release detected after  $\tau_p$ . The continued release of linker from clusters during particle growth moreover indicates that they play a direct role in particle growth – not merely serving as nucleation sites followed by monomer attachment, as this would rapidly lower the concentration of mobile imidazole in the solution. Through correlation of the area of the olefinic imidazole resonance with that of the exchangeable protons we

were able to assign the released species as 2-MelmH<sub>2</sub><sup>+</sup> (Figure 1.i.). This aligns well with a kinetic model presented by Yeung et al., who predicted that rapid equilibration of monomeric complexes leads to the formation of oligomeric clusters in a pre-equilibrium state.<sup>41</sup> Since these clusters contain excess protonated ligand as compared to the final ZIF-8 stoichiometry, Zn(Melm)<sub>2</sub>, further growth involves the release of 2-MelmH<sub>2</sub><sup>+</sup> through condensation. The increase in mobile imidazole detected by NMR during particle growth is therefore directly related to condensation reactions from within and between clusters. This implies that particle growth is driven by the association of prenucleation clusters rather than incorporation of monomeric species or cluster dissolution.

After the onset of particle growth at  $\tau_p$ , SLS and DLS reveal an initial exponential increase in particle size, that fits to the classic JMAK model (Fig. 1a and 1b). Subsequently, at  $\tau_{\text{ZIF-8}}$ , the crystalline phase of ZIF-8 was detected by SHS with a 35 second delay. The structural assignment of ZIF-8 was further corroborated by the SHS depolarization ratio, aligning with the I-43m space group of the crystal lattice (Fig. 1c). This observed delay in detection is reminiscent of the findings of Cravillon et al., who reported a similar lag in detection of ZIF-8's crystalline phase using synchrotron WAXS in comparison with SAXS. Since it was not clear whether this difference could be attributed to the presence of an amorphous precursor, or merely to differences in sensitivity between both techniques, the authors were not able to draw definitive conclusions about the presence of amorphous precursor particles in the nucleation pathway of ZIF-8. In this study, SHS, akin to WAXS, demonstrated exclusive sensitivity to the crystalline form of ZIF-8, but exhibits limited sensitivity compared to SLS and DLS. Through theoretical and experimental characterization of the second harmonic efficiency of crystalline ZIF-8, we estimated a minimum detectable diameter via SHS of  $x$  nm, which is significantly smaller than the particle size of  $x$  nm detected by DLS at  $\tau_{\text{ZIF-8}}$  (see ESI.5). This implies that the particles detected by DLS are not entirely crystalline at this point. By incorporating THS, which, unlike SHS, is sensitive to amorphous phases, we were able to unambiguously confirm the presence of an amorphous precursor phase. The amorphous nature of this precursor phase was corroborated through depolarization measurements (Fig. 1c). Through analysis of the relative progression of SHS and THS, we were moreover able to separate the evolution of the amorphous and crystalline fraction over time, thereby providing insight into the role of the precursor phase in the nucleation mechanism of ZIF-8 (Fig. 1d). Our analysis demonstrates that the formation of amorphous precursor particles precedes crystalline ZIF-8 formation. These precursor particles do not merely act as short-lived intermediates but rather drive the nucleation and growth process throughout the exponential growth stage. Growth rate analysis indeed reveals that the amorphous phase consistently outpaces the crystalline phase during this stage (see ESI 3.9). As detailed above, NMR data indicate an increase in mobile ligand, consistent with pre-nucleation cluster association, even before the appearance of crystalline ZIF-8. This implies that amorphous precursor particles are formed through cluster association and subsequently transition into crystalline ZIF-8. The uninterrupted release of 2-MelmH<sub>2</sub><sup>+</sup> into the solution, even after the onset of crystallization, suggests that nucleation and growth of the crystalline framework occurs through condensation and intraparticle reorganization rather than through dissolution and monomer attachment.

At  $\tau_{\text{OR}}$  (200 seconds), the growth mechanism shifts from exponential growth to diffusion controlled Ostwald ripening. This shift is evidenced by a Lifshitz-Slyozov fit of the DLS data (Fig. 1b), and is marked by a reversal of the flux of mobile ligands observed by NMR (Fig. 1e), which now shows a decrease. Concurrently, the rise in proton concentration registered by NMR starts to level off. This implies that further growth predominantly occurs through incorporation of monomeric species from solution through Ostwald ripening, rather than through association-condensation. The amorphous fraction, as detected by THS (Fig. 1d), reaches a maximum at  $\tau_{\text{OR}}$ , after which it starts to decrease. Synchrotron-based X-ray measurements showed a further increase in crystallinity throughout this stage,<sup>29,43</sup> suggesting intraparticle reorganization. Around 350 seconds, the amorphous fraction is fully depleted,

while the proton concentration registered by NMR plateaus. At this time, the reservoir of prenucleation cluster building blocks has fully transformed into crystalline ZIF-8. Beyond this point, growth proceeds exclusively through the incremental addition of monomers.

Our observations are in line with a four-step nucleation and growth mechanism, summarized in Fig. 2. Immediately after mixing, a population of prenucleation clusters, with a stable size of a few nanometres, forms alongside with a variety of Zn-linker complexes, mainly consisting of monomeric

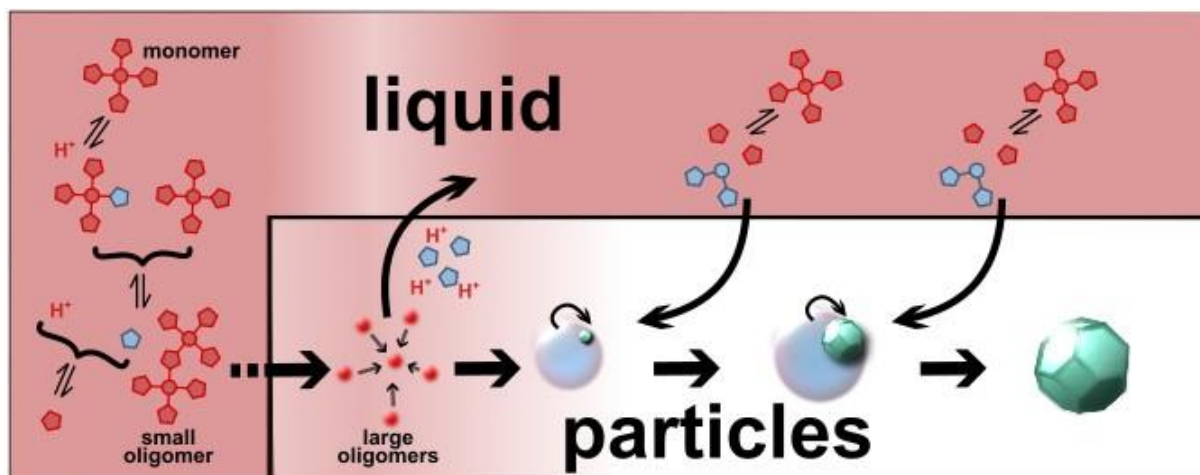


Figure 2 Scheme showing the three-step nonclassical nucleation mechanism as derived from our observations through NMR and HLS

species. These prenucleation clusters are positively charged and contain an excess of ligand and protons compared to the final structure of ZIF-8. These clusters are the building blocks for the formation of amorphous precursor particles that grow through association of pre-nucleation clusters. The growth of amorphous precursor particles is accompanied by the release of excess ligand and protons into the surrounding solution, resulting in the formation of larger, net neutral charge particles. Subsequently, nucleation of crystalline ZIF-8 takes place inside these amorphous precursor particles, after which crystal growth ensues through intraparticle reorganization. When the reservoir of oligomeric clusters becomes depleted, the growth mechanism switches to Ostwald ripening, and further growth occurs through incorporation of charge neutral monomeric species from solution. Concurrently, an increase in crystallinity through intraparticle reorganization takes place.

The different steps of the nonclassical pathway can be understood from their progression in terms of charge and stoichiometry, transitioning from positively charged, overstoichiometric species to the final stoichiometric composition of the neutral charge crystalline phase. An important aspect not directly observed in our study, but inherently present and influencing the system, involves the positively charged prenucleation species and their counter ions, notably nitrate ions ( $-\text{NO}_3$ ), which likely serve as charge compensating species. Although our methods do not detect these ions, their presence and role in balancing the positive charge of the clusters are expected to significantly impact the nucleation mechanism. A study by Priandani et al. on the modulation of ZIF-8 synthesis with sodium chloride supports this notion, highlighting how varying amounts of NaCl can lead to distinct changes in crystal size and morphology, akin to those observed in solvothermal synthesis with  $\text{ZnCl}_2$ . This opens up the exciting possibility of rational crystallization control through interaction with intermediate species in the nucleation pathway.

## Conclusion

In conclusion, our research provides unprecedented insights into the crystallization process of ZIF-8, delineating a four-step nucleation and growth model. This model progresses from the formation of positively charged prenucleation clusters to amorphous precursor particles, leading to nucleation of the crystalline phase and culminating in crystal growth via intraparticle reorganization and Ostwald ripening. Our findings emphasize the critical role of integrating in-situ chemical and structural analysis to unravel the complex interplay between structure and chemistry that drives crystallization of MOFs. By detecting the chemical nature of the involved species, our approach not only deepens our understanding of the crystalline phase formation of ZIF-8 but also provides handles for controlling crystallization in MOFs through the manipulation of precursor pathways via various external conditions. We are convinced that our approach holds potential to offer distinctive insights into the complex nucleation and growth mechanisms of related materials, encompassing MOFs, zeolites, and myriad other materials. Also for proteins, where amorphous liquid-like precursors often precede supramolecular order, our approach is highly promising to disentangle the underlying mechanisms crystallization and aggregation.

## 6. Materials and methods

### *Materials*

Zinc nitrate hexahydrate (98%, extra pure) was purchased from Acros Organics. 2-methylimidazole (99%) and Methanol (ACS spectrophotometric grade, >99.9%) were purchased from Sigma-Aldrich. Methanol was further purified through disposable syringe filters (Chromafil®, Glass fiber + Polyester filter, 0.20 µm pore size) purchased through Macherey-Nagel. The measurement cuvettes (High Precision Cell (QS), Light path 10x10mm) used for the *in situ* measurements were purchased through HellmaAnalytics.

The methanolic ZIF-8 synthesis was performed according to a published procedure.<sup>6,10,29</sup> While the ZIF-8 was synthesized both *in situ* and *ex situ*, the procedure was highly similar. Two stock solutions were prepared, one containing the zinc source ( $\text{Zn}(\text{NO}_3)_2 \cdot 6\text{H}_2\text{O}$ ) and another containing 2-methylimidazole ( $\text{C}_4\text{H}_6\text{N}_2$ ). The two solutions were mixed to start the crystallization. The ratio of addition for the synthesis was determined by the desired molar ratio in the form of 1:x:1000 for Zn:2-methylimidazole:methanol. For the *ex situ* synthesis the solution mixture was stirred for 24 hours at room temperature to allow nucleation and growth of the crystals. Afterwards, the crystals were separated from the reaction mixture by centrifugation and washed with methanol. This procedure was repeated 3 times followed by a drying period under vacuum at 50°C. The *in situ* synthesis followed similar procedure, however an automated syringe system was used to mix the two stock solutions and inject the mixture into the quartz measurement cell. The start of the mixing and subsequent injection into the measurement cell was used as the starting time of the reaction, but it took 5 seconds to complete injection and fill the measurement cell.

### *HRS and SLS setup*

The experimental setup to perform the light scattering measurements was described elsewhere.<sup>32,38</sup> For our use, this setup was slightly modified. This setup uses a femtosecond laser (Insight DS+, Spectra-Physics) with tunable wavelength ranging from 680 to 1300 nm, as a high-power light source. For the measurements, a fundamental wavelength of 1300 nm was used at a frequency of 80 MHz width pulse widths of 120 fs. The intensity variation of the incident light and the vertical polarization was accomplished by the combination of an achromatic half-wave plate and a Glan-Taylor polarizer. The

light is subsequently focused into a 10 x10 mm quartz cuvette containing the solution by an aspheric lens (A220TM, Thorlabs). The resulting beam waist of the focused beam is around 8  $\mu\text{m}$  and a Rayleigh length of about 190  $\mu\text{m}$ .

A secondary laser was coupled into the system for static light scattering. Again, a half-wave plate and a Glan-Taylor polarizer combination was used to ensure a vertical polarization and power modulation of the incoming light. The secondary beam was guided and aligned to ensure the same focus positions as the primary incoming beam. However, obtained focus size was different compared to the primary beam due to differences in beam diameter and quality.

The scattered light was collected under 90° and subsequently collimated and focused onto the slit of a spectrograph (Bruker IS 500) attached to an EMCCD camera (Ixon 897, Andor Oxford instruments). To collect the full image of the focal point onto the slit, a rotation of the image by 90° was achieved by a set of mirrors in a periscope system. Before the spectrograph, a Wollaston prism was placed to separate the scattered light into its vertical and horizontal polarized components. Using the grating (150 l/mm, 300 blaze) in the spectrograph allowed to separate the incoming light, allowing us to measure simultaneously the depolarization ratio for SHS, THS and SLS. The temporal resolution of the in-situ measurements were limited, due to the low scattering efficiency of SHS and THS. Therefore, the data acquisition times were always kept at 4s.

#### *Powder X-ray Diffraction*

X-ray diffraction (XRD) patterns were obtained on a Malvern PANalytical Empyrean diffractometer, equipped with a PIXcel3D solid-state detector using a Cu anode (using Ka1 and Ka2). The powder samples were loaded onto a 48-well sample holder and X-ray diffractograms were recorded at room temperature in a transmission geometry within a 1.3 - 45° 2 $\theta$  range using a step size of 0.013°.

#### *In situ NMR measurements*

*In situ*  $^1\text{H}$  NMR measurements were performed on a Bruker 800 MHz Avance Neo spectrometer equipped with a 5mm  $^1\text{H}/^2\text{H}/\text{X}$  BBO probehead ( $^1\text{H}$  Larmor frequency 801.25 MHz). Equal volumes of 2-methyl imidazole and zinc nitrate solutions in deuterated methanol (Methanol- $\text{D}_4$ , Sigma Aldrich) were mixed in a 1:4 molar ratio in a 5 mm NMR tube (Norrel) and inserted into the probehead.  $^1\text{H}$  spectra were acquired every 5 s with an RF pulse of 18 kHz, an acquisition time of 1s and relaxation delay of 4s. The spectra were processed and integrated using Bruker Topspin 4.0.9 software.

#### *Ex-situ NMR measurements*

Concentrations of linker molecule (2-methylimidazole, 2-Me-ImH) were determined through  $^1\text{H}$  nuclear magnetic resonance (NMR) measurements using a Magritek SpinSolve 80 Carbon benchtop spectrometer ( $^1\text{H}$  basic frequency 80.478 MHz). Prior to the measurements of the ZIF-8 samples, a calibration curve was generated to determine the accuracy and precision of concentration determination through NMR. The internal standard employed for this purpose was tetramethylammonium bromide (TMAB, stock solution of 49.52 mM in  $\text{D}_2\text{O}$ ). Acquisition parameters for all recorded datasets were: relaxation delay time = 15 s, pulse angle = 30°, acquisition time = 3.2 s, number of scans = 32, dummy scans = 0, total measurement time = 8 min. Processing of the NMR spectra were performed using Bruker's TopSpin (version 4.1.3) and involved zero-filling the free induction decay (FID) signal up to a total of 256k real datapoints (*si* 256k), exponential multiplication (*lb* 0.3 Hz), Fourier transform, automatic phase correction and baseline correction. Analysis of the spectra is described in the paragraph below.

## 1. Calibration curve

2-Me-ImH samples were weighed on an analytical balance (Mettler Toledo XS105). The weighted samples were dissolved in 650  $\mu\text{L}$  deuterated solvent (600  $\mu\text{L}$   $\text{D}_2\text{O}$ , Sigma Aldrich, 99 atom %D, containing the TMAB + 50  $\mu\text{L}$   $\text{D}_2\text{SO}_4$  solution, Sigma Aldrich 96-98 wt. % in  $\text{D}_2\text{O}$ , 99.5 atom %D). Clear solutions were obtained through shaking, vortex and sonification. The range of 2-Me-ImH concentrations for the calibration curve was [22.7 mM, 142.8 mM]. The second data point was replicated ( $n = 3$ ), to allow estimation of weighing and operator error. The NMR tubes were filled with 500  $\mu\text{L}$  of the solution to allow optimal shimming of the sample. Methyl signals of both TMAB and 2-Me-ImH were integrated in an unbiased way by the following two steps: 1. peak center and full-width at half maximum (FWHM) were determined with the *peakw* command, 2. FWHM was multiplied by nine and both added to and subtracted from the peak center defining the integration range. Simultaneously, the signal-to-noise ratio (SINO) of the 2-Me-ImH methyl signal was computed to ensure sufficient quality of the recorded spectra. Next, the integration values were normalized to their respective proton count (TMAB = 12 H's, 2-Me-ImH = 3 H's). Finally, the calculated ratios (2-Me-ImH/TMAB) between integration values of 2-Me-ImH and TMAB were compared with the expected ratios based on their relative concentrations.

## 2. Sample measurements

The ZIF-8 sample was weighed in quintuplicate followed by computation of the mean mass of the sample. Subsequently, the sample was dissolved in 650  $\mu\text{L}$  deuterated solvent (600  $\mu\text{L}$   $\text{D}_2\text{O}$  containing the TMAB + 50  $\mu\text{L}$   $\text{D}_2\text{SO}_4$ ). The presence of sulfuric acid disrupts the interaction between the  $\text{Zn}^{2+}$  metal nodes and the linker molecule. Clear solutions were obtained through shaking, vortex and sonification. The same analysis protocol was followed for the calibration curve. The final calculated ratio was corrected using the calibration curve.

## 6. Acknowledgments

C.K. acknowledges the Flemish Government for long-term Methusalem structural funding. E.B., and C.K. acknowledge joint funding by the Flemish Science Foundation (FWO; G083318N) and the Austrian Science Fund (FWF) (funder ID 10.13039/501100002428, project ZeoDirect I 3680-N34). E.B. acknowledges FWO for a “Krediet aan navorsers” 1.5.061.18N. NMRCoRe is supported by the Hercules Foundation (AKUL/13/21), by the Flemish Government as an international research infrastructure (I001321N), and by Department EWI via the Hermes Fund (AH.2016.134). The authors acknowledge FWO Vlaanderen and the teams at DUBBLE beamlines (ESRF, Grenoble) for financial and experimental support, respectively.

## 7. References

- 1 S. M. Moosavi, A. Nandy, K. M. Jablonka, D. Ongari, J. P. Janet, P. G. Boyd, Y. Lee, B. Smit and H. J. Kulik, *Nat. Commun.*, 2020, **11**, 1–10.
- 2 M. Eddaoudi, D. B. Moler, H. Li, B. Chen, T. M. Reineke, M. O’Keeffe and O. M. Yaghi, *Acc. Chem. Res.*, 2001, **34**, 319–330.
- 3 M. J. Van Vleet, T. Weng, X. Li and J. R. Schmidt, , DOI:10.1021/acs.chemrev.7b00582.
- 4 A. Deacon, L. Briquet, M. Malankowska, S. Rudi, T. Hyde, T. Johnson, F. Massingberd-mundy, H. Cavaye, J. Coronas and S. Poulston, *Commun. Chem.*, 2022, **5**, 1–10.
- 5 X. Liu, S. W. Chee, S. Raj, M. Sawczyk, P. Král and U. Mirsaidov, *Proc. Natl. Acad. Sci. U. S. A.*, , DOI:10.1073/pnas.2008880118.
- 6 J. Cravillon, S. Münzer, S. J. Lohmeier, A. Feldhoff, K. Huber and M. Wiebcke, *Chem. Mater.*, 2009, **21**, 1410–1412.
- 7 J. Cravillon, C. A. Schröder, R. Nayuk, J. Gummel, K. Huber and M. Wiebcke, *Angew. Chemie - Int. Ed.*, 2011, **50**, 8067–8071.
- 8 J. Cravillon, C. A. Schröder, H. Bux, A. Rothkirch, J. Caro and M. Wiebcke, *CrystEngComm*, 2012, **14**, 492–498.
- 9 M. W. Terban, D. Banerjee, S. Ghose, B. Medasani, A. Shukla, B. A. Legg, Y. Zhou, Z. Zhu, M. L. Sushko, J. J. De Yoreo, J. Liu, P. K. Thallapally and S. J. L. Billinge, *Nanoscale*, 2018, **10**, 4291–4300.
- 10 J. Cravillon, R. Nayuk, S. Springer, A. Feldhoff, K. Huber and M. Wiebcke, *Chem. Mater.*, 2011, **23**, 2130–2141.
- 11 F. Carraro, J. D. Williams, M. Linares-Moreau, C. Parise, W. Liang, H. Amenitsch, C. Doonan, C. O. Kappe and P. Falcaro, *Angew. Chemie*, 2020, **132**, 8200–8204.
- 12 E. L. Bustamante, J. L. Fernández and J. M. Zamaro, *J. Colloid Interface Sci.*, 2014, **424**, 37–43.
- 13 X. Wu, H. Yue, Y. Zhang, X. Gao, X. Li, L. Wang, Y. Cao, M. Hou, H. An, L. Zhang, S. Li, J. Ma, H. Lin, Y. Fu, H. Gu, W. Lou, W. Wei, R. N. Zare and J. Ge, *Nat. Commun.*, 2019, **10**, 1–8.
- 14 I. H. Lim, W. Schrader and F. Schu, , DOI:10.1021/acs.chemmater.5b00614.
- 15 Y. Zhu, J. Ciston, B. Zheng, X. Miao, C. Czarnik, Y. Pan and R. Sougrat, 2017, **16**, 4–9.
- 16 J. P. Patterson, P. Abellan, M. S. Denny, C. Park, N. D. Browning, S. M. Cohen, J. E. Evans and N. C. Gianneschi, , DOI:10.1021/jacs.5b00817.
- 17 B. Jin, S. Wang, D. Boglaienko, Z. Zhang, Q. Zhao, X. Ma, X. Zhang and J. J. De Yoreo, *J. Cryst.*



- Growth*, 2023, **603**, 126989.
- 18 S. Saha, S. Springer, M. E. Schweinefuß, D. Pontoni, M. Wiebcke and K. Huber, *Cryst. Growth Des.*, 2016, **16**, 2002–2010.
  - 19 S. Saha, M. Wiebcke and K. Huber, *Cryst. Growth Des.*, 2018, **18**, 4653–4661.
  - 20 A. F. Ogata, A. M. Rakowski, B. P. Carpenter, D. A. Fishman, J. G. Merham, P. J. Hurst and J. P. Patterson, *J. Am. Chem. Soc.*, 2020, **142**, 1433–1442.
  - 21 M. Kumar, R. Li and J. D. Rimer, *Chem. Mater.*, 2016, **28**, 1714–1727.
  - 22 J. D. Rimer and M. Tsapatsis, *MRS Bull.*, 2016, **41**, 393–398.
  - 23 R. Jain, A. J. Mallette and J. D. Rimer, *J. Am. Chem. Soc.*, 2021, **143**, 21446–21460.
  - 24 K. N. Olafson, R. Li, B. G. Alamani and J. D. Rimer, *Chem. Mater.*, 2016, **28**, 8453–8465.
  - 25 J. D. Rimer, A. Chawla and T. T. Le, *Annu. Rev. Chem. Biomol. Eng.*, 2018, **9**, 283–309.
  - 26 M. Filez, C. Caratelli, M. Rivera-torrente, A. J. R. Heck, V. Van, M. Bert, M. Filez, C. Caratelli, M. Rivera-torrente, F. Muniz-miranda, M. Hoek, M. Altelaar, A. J. R. Heck, V. Van Speybroeck and B. M. Weckhuysen, *Cell Reports Phys. Sci.*, 2021, **2**, 100680.
  - 27 Z. Öztürk, M. Filez and B. M. Weckhuysen, *Chem. - A Eur. J.*, 2017, **23**, 10915–10924.
  - 28 H. H. M. Yeung, A. F. Sapnik, F. Massingberd-Mundy, M. W. Gaultois, Y. Wu, D. A. X. Fraser, S. Henke, R. Pallach, N. Heidenreich, O. V. Magdysyuk, N. T. Vo and A. L. Goodwin, *Angew. Chemie - Int. Ed.*, 2019, **58**, 566–571.
  - 29 J. Cravillon, C. A. Schröder, R. Nayuk, J. Gummel, K. Huber and M. Wiebcke, *Angew. Chem. Int. Ed. Engl.*, 2011, **50**, 8067–71.
  - 30 A. R. Dok, T. Legat, Y. de Coene, M. A. van der Veen, T. Verbiest and S. Van Cleuvenbergen, *J. Mater. Chem. C*, 2021, **9**, 11553–11568.
  - 31 S. Van Cleuvenbergen, Z. J. Smith, O. Deschaume, C. Bartic, S. Wachsmann-Hogiu, T. Verbiest and M. A. van der Veen, *Nat. Commun.*, , DOI:10.1038/s41467-018-05713-4.
  - 32 N. Van Steerteghem, K. Clays, T. Verbiest and S. Van Cleuvenbergen, *Anal. Chem.*, 2017, **89**, 2964–2971.
  - 33 S. Van Cleuvenbergen, I. Stassen, E. Gobechiya, Y. Zhang, K. Markey, D. E. De Vos, C. Kirschhock, B. Champagne, T. Verbiest and M. A. Van Der Veen, *Chem. Mater.*, 2016, **28**, 3203–3209.
  - 34 V. R. Thierry Verbiest, Koen Clays, *Second-order Nonlinear Optical Characterization Techniques Ie*, CRC Press, 2009.
  - 35 K. D. M. Harris, C. E. Hughes, P. A. Williams and R. Gregory, 2017, 137–148.
  - 36 C. E. Hughes, P. A. Williams, B. M. Kariuki and K. D. M. Harris, 2018, 1–6.
  - 37 N. Pellens, N. Doppelhammer, S. Radhakrishnan, K. Asselman, C. V. Chandran, D. Vandenaabeele, B. Jakoby, J. A. Martens, F. Taulelle, E. K. Reichel, E. Breynaert and C. E. A. Kirschhock, , DOI:10.1021/acs.chemmater.2c00418.
  - 38 M. Moris, M. P. Van Den Eede, G. Koeckelberghs, O. Deschaume, C. Bartic, S. Van Cleuvenbergen, K. Clays and T. Verbiest, *Commun. Chem.*, 2019, **2**, 1–9.
  - 39 M. Moris, M. P. Van Den Eede, G. Koeckelberghs, O. Deschaume, C. Bartic, K. Clays, S. Van

- Cleuvenbergen and T. Verbiest, *Macromolecules*, 2020, **53**, 9513–9520.
- 40 F. Wang, V. N. Richards, S. P. Shields and W. E. Buhro, *Chem. Mater.*, 2014, **26**, 5–21.
- 41 H. H. -M. Yeung, A. F. Sapnik, F. Massingberd-Mundy, M. W. Gaultois, Y. Wu, D. A. X. Fraser, S. Henke, R. Pallach, N. Heidenreich, O. V. Magdysyuk, N. T. Vo and A. L. Goodwin, *Angew. Chemie*, , DOI:10.1002/ange.201810039.
- 42 C. Grunewald, R. Seidel and A. Chapartegui-arias, 2020, 8–11.
- 43 S. R. Venna, J. B. Jasinski and M. A. Carreon, *J. Am. Chem. Soc.*, 2010, **132**, 18030–18033.